Maximum Stiffness of Impact-Robust Actuators in Highly Dynamic Robotics Tasks: Application to Series Elastic Actuator Design

Anton Shu[1,2], Florian Loeffl[1], Alexander Kolb[1], Konrad Fründ[1], David Wandinger[1], Fabian Beck[1], Jens Reinecke[1,3], Markus Grebenstein[1,4], Marco Hutter[2] and Jinoh Lee[1,5]

***Abstract*—Highly dynamic motions such as running expose legged robot actuators to substantial impact torques, necessitating impact-resilient or impact-robust designs. Accordingly, actuator design must explicitly account for these impact robustness requirements. We present solutions for the impact-induced peak torque at the gearbox, where we analyze applicable contact time and parameter sensitivity. From these, we derive algebraic inequalities to determine the maximum stiffness of series elastic actuators that exhibit impact robustness. Derived from a time-domain solution of the post-impact dynamics, the proposed closed-form inequalities incorporate gearbox peak torque, reduction ratio, motor and link inertia, operational torque acting before and during impact, as well as impact impulse. We demonstrate this method by designing a humanoid actuator featuring both a novel 14 J hollow-shaft spring with 546 Nm/rad, and a conceptual axial torque-overload breakaway disk for added safety. Experimental evaluation of the impact response validates our impact-torque prediction for two different contact-time regimes, three different link inertia settings and two different stiffness settings.**

***Index Terms*—Actuation and Joint Mechanisms, Compliant Joints and Mechanisms, Mechanism Design, Humanoid Robot Systems, Legged Robots**

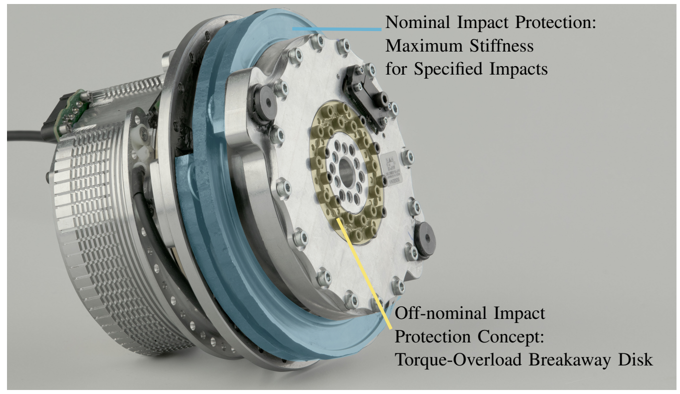

Fig. 1. Impact-robust actuator featuring a maximum stiffness spring and an easily replaceable torque-overload breakaway disk.

I. Introduction

In fast legged locomotion, impacts on the actuation system are both unavoidable [1] and possibly fast. Biomechanical data suggest that contact durations until the initial peak force range between 4 and 50 ms in heel strike running [2], [3]. In robotic systems, precautions against such nominal impacts are taken at the actuator level [4], [5], the leg level, such as the mass distribution [6] or the foot elasticities [7], or the reaction strategies [8]. While reaction strategies are suited to longer contacts, and leg-level resolutions can be found for specific applications, impact resilience or impact robustness at actuator level offers greater general applicability.

One option to increase impact robustness is to include passive elasticities, as in series elastic actuators (SEAs), where a spring acts as a low-pass filter to shock loads and hence reduces the peak torque within the actuator [9]. Additional benefits include the possibility of utilizing embedded natural dynamics [10] or measuring torques via the elastic element. However, the spring generally lowers the mechanical bandwidth of the actuator [11], which limits dynamic responsiveness and the achievable closed-loop control bandwidth [12]. Hence, for highly dynamic tasks, the maximum stiffness that still guarantees impact robustness is desirable. Another option is the usage of low-geared actuators without a dedicated spring in a quasi-direct drive (QDD), also known as proprioceptive actuator [13], [6], which have high mechanical bandwidth but limited impact robustness [14]. For insights into their short-contact-time impact response, these could be modeled as SEAs with the physical gear stiffness as elasticity.

To select actuator parameters for robustness against impacts, several qualitative guidelines recommend reducing reflected inertia [6], [15] or stiffness [4], [5], [15]. To quantitatively determine the stiffness for a given inertia, dynamic simulations with different stiffness settings are performed at the actuator level [4], [5] or the leg level [15]. While simulations effectively validate existing designs, exploring a wider parameter space, such as varying inertia, gear ratio, and stiffness simultaneously, remains challenging. For the derivation of new designs, closed-form equations reduce the number of needed design iterations and speed up the design process. An example is the pocket-calculator-compatible design guide for differential elastic actuators [16], which reduces design process complexity but does not provide deep insight into the method, such as contact time applicability bounds, sensitivity or comparison to energy-based calculations.

In general, a higher impact robustness results in a higher required energy capacity of the spring. The induced increase in weight and volume is limited by integrating the spring

Manuscript received: January 30, 2026; Revised: May 13, 2026; Accepted: June 24, 2026. This paper was recommended for publication by Editor Cosimo Della Santina upon evaluation of the Associate Editor and Reviewers' comments. This was partly supported by the Council of Science & Technology(NST) grant by the Korea government No. GTL25041-000. (*Corresponding author: Anton Shu.*)

[1]German Aerospace Center (DLR), Institute of Robotics and Mechatronics, Germany anton.shu@dlr.de, [2]Robotic Systems Lab, ETH Zurich, Switzerland, [3] Agile Robots SE, Germany, [4]Monash University, Australia, [5]KAIST, South Korea.

Digital Object Identifier (DOI): 10.1109/LRA.2026.3710324.

in the actuator [11], optimization of the spring layout [17], [18], and location [19],[20],[21]. However, overly conservative nominal impact assumptions can make the design infeasible. For these cases, couplings can offer additional physical impact protection against rare off-nominal impacts such as erroneous handling, falling, or externally caused collisions [22],[23],[24].

In our assessment, an exemplary application of a straightforward method for determining the maximum stiffness of SEAs under short-contact impacts is lacking together with insights into this method that could be provided by comparing with an energy based computation for stoppage at maximum motor speed, contact-time applicability bounds and a sensitivity analysis.

Hence, this letter offers the following contributions:

- Comparison of a method to directly calculate the maximum stiffness of SEAs that maintains robustness against short-contact-time impacts when applied to specified impulses with the same method when applied to sudden stoppage of the link at maximum speed.
- Analysis of admissible contact duration and sensitivity to actuator parameters of the peak impact torque.
- Implementation of the method on an actuator prototype that includes a novel high-energy-density spring design for radial mounting and a concept for a torque-overload breakaway disk as an additional safety layer, shown in Fig. 1

The remainder of the letter is structured as follows: first, Sec. II introduces and compares two methods for calculating the stiffness. Sec. III introduces an actuator design where one of these methods is applied, along with its spring and torque-overload protection. Sec. IV shows experimental evaluation results and Sec. V concludes this letter.

II. Maximum Stiffness Design Methods

This section presents two methods for computing SEA stiffness which maintains impact robustness. We present analytical models for the actuator and impact dynamics, and derive a formulation for the peak torque with a sensitivity analysis. The first derived method guarantees robustness against specified impacts. The second derived method needs fewer assumptions and aims to balance impact robustness and maximum motor speed. Finally, both methods are discussed and compared.

A. Gearbox Interface Torque

Excessive gearbox interface torque τ_u poses a risk to the gearbox and other actuator components. Fig. 2 illustrates the SEA model, where the torque τ_u interfaces the gearbox and the link. In this system, electromagnetic torque τ_m acts on the rotor, while external torque τ_ext acts on the link which has inertia I_u and velocity $\dot{q}_\mathrm{u}$. The link motion is transmitted through the spring with stiffness K and gearbox with reduction ratio N to the rotor with inertia I_r and velocity $\dot{q}_\mathrm{r}$. The governing equations of motion are given as

$$I_\mathrm{r}\ddot{q}_\mathrm{r} + B_\mathrm{r}\dot{q}_\mathrm{r} = \tau_\mathrm{m} + N^{-1}\tau_\mathrm{u}, \quad (1)$$

$$B_\mathrm{s}(\dot{q}_\mathrm{u} - N^{-1}\dot{q}_\mathrm{r}) + K(q_\mathrm{u} - N^{-1}q_\mathrm{r}) = \tau_\mathrm{u}, \quad (2)$$

$$I_\mathrm{u}\ddot{q}_\mathrm{u} + B_\mathrm{u}\dot{q}_\mathrm{u} = -\tau_\mathrm{u} + \tau_\mathrm{ext}, \quad (3)$$

where B_i denotes damping coefficients and its subscript $i \in \{\mathrm{r}, \mathrm{s}, \mathrm{u}\}$ denotes rotor, spring, and link, respectively.

An external impact imparts an angular impulse p_ext to the link that we model as a half-sine wave with contact duration Δ on τ_ext using the Heaviside function $H(t)$ as

$$\tau_\mathrm{ext}(t) = \sin\left(\frac{\pi t}{\Delta}\right)\frac{\pi}{2\Delta}(1 - H(t-\Delta))p_\mathrm{ext}. \quad (4)$$

To solve (1)-(4) the motor and link dynamics (1)-(3) are expressed in the Laplace domain with the Laplace variable s as $P_\mathrm{r}(s) = \left(I_\mathrm{r}s^2 + B_\mathrm{r}s\right)^{-1}$, $P_\mathrm{s}(s) = (B_\mathrm{s}s + K)^{-1}$ and $P_\mathrm{u}(s) = \left(I_\mathrm{u}s^2 + B_\mathrm{u}s\right)^{-1}$ similar to [25]. With these, we define the robustness transfer function $R(s)$ that relates τ_ext to τ_u, similar to [16], as

$$R(s) = \frac{\tau_\mathrm{u}}{\tau_\mathrm{ext}} = \frac{N^2P_\mathrm{u}}{N^2P_\mathrm{u} + N^2P_\mathrm{s} + P_\mathrm{r}}. \quad (5)$$

Together with (4) and (5), we find the gearbox interface torque after an impulse for a known Δ as $\tau_{\mathrm{u,imp},\Delta}(t)$ through the inverse Laplace transform $\mathcal{L}^{-1}$ as

$$\tau_{\mathrm{u,imp},\Delta}(t) = \mathcal{L}^{-1}\left(R(s)\frac{1+e^{-\Delta s}}{2+2\left(\Delta/\pi\right)^2}p_\mathrm{ext}\right). \quad (6)$$

In case of unknown Δ the limit of $\Delta \to 0$ can be used as

$$\tau_{\mathrm{u,imp},0}(t) = \mathcal{L}^{-1}\left(R(s)p_\mathrm{ext}\right). \quad (7)$$

We assume that the impact does not influence control action and use the linearity of our system to add the operational torques that act before and during the impact on the gearbox interface $\tau_\mathrm{u,op}$ as

$$\tau_\mathrm{u}(t) = \tau_\mathrm{u,imp}(t) + \tau_\mathrm{u,op}. \quad (8)$$

We use impulse or transferred momentum instead of sudden accelerations or shock loads, since we consider I_u a design parameter of robotic systems that can shape the impact load. One possibility of computing p_ext in a multi-body system is given by [26]. Equation (6) is a differentiable algebraic expression for $\tau_{\mathrm{u,imp},\Delta}(t)$ after an impact as a function of actuator parameters I_i, B_i, K, N and impulse parameters Δ,p_ext. It is useful to simulate the effect of single impacts without solver inaccuracies.

B. Peak Impact Torque

We approximate an upper bound on the peak impact torque $\tau_\mathrm{u,peak}$ by neglecting damping. First, we determine the eigenfrequency of the undamped system ω as

$$\omega = \sqrt{K\left(\frac{1}{N^2I_\mathrm{r}} + \frac{1}{I_\mathrm{u}}\right)}, \quad (9)$$

and substitute Δ by the period factor $a = \frac{\Delta\omega}{\pi}$. Then, we derive the undamped impulse response $\hat{\tau}_{\mathrm{u,imp},\Delta}(t)$ from (6) with the transient response $F(t)$ and long-term response $G(t)$ as

$$\hat{\tau}_{\mathrm{u,imp},\Delta}(t) = \tau_\mathrm{u}(t)\Big|_{B_i=0} = \begin{cases} \frac{Kp_\mathrm{ext}}{2I_\mathrm{u}\omega}F(t) & ,t < \Delta \\ \frac{Kp_\mathrm{ext}}{2I_\mathrm{u}\omega}G(t) & ,t > \Delta \end{cases}, \quad (10)$$

$$F(t) = \frac{\sin(\omega t) - a\sin\left(\frac{\omega}{a}t\right)}{1-a^2}, G(t) = \frac{\sin(\omega t) - \sin(\pi a - \omega t)}{1-a^2}.$$

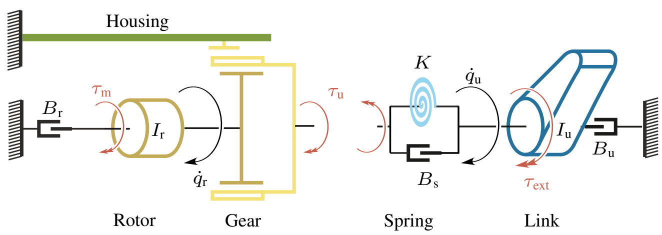

Fig. 2. Schematic diagram of the SEA model structure with gearbox interface torque τ_u.

Both $F(t)$ and $G(t)$ are bounded for $a<1$. By determining the time of the maximum and substituting for t respectively we find

$$\frac{\hat{\tau}_{\mathrm{u,imp},\Delta}(t)}{p_\mathrm{ext}} \leq \begin{cases} \frac{K}{2I_\mathrm{u}} \frac{\sin\left(\frac{2\pi a}{a+1}\right)-a\sin\left(\frac{2\pi}{a+1}\right)}{\omega(1-a^2)} & ,t<\Delta \\ \frac{K}{2I_\mathrm{u}} \frac{2\cos\left(\frac{\pi a}{2}\right)}{\omega(1-a^2)} & ,t>\Delta \end{cases}. \tag{11}$$

For $a<1$ the bound for $t>\Delta$ dominates, hence the upper bound on $\hat{\tau}_{\mathrm{u,imp},\Delta}(t)$ with $\hat{\tau}_{\mathrm{u,peak},\Delta}$ is given as

$$\hat{\tau}_{\mathrm{u,peak},\Delta} = \frac{K p_\mathrm{ext}}{I_\mathrm{u}\omega} \frac{\pi^2 \cos\left(\frac{\Delta\omega}{2}\right)}{\pi^2-(\Delta\omega)^2} + \tau_\mathrm{u,op} \quad ,\Delta<\frac{\pi}{\omega}. \tag{12}$$

The limit case for $\Delta\to 0$ is given as

$$\begin{aligned} \hat{\tau}_\mathrm{u,peak,0} &= \lim_{\Delta\to 0}\left(\hat{\tau}_{\mathrm{u,peak},\Delta}\right) \\ &= \sqrt{\frac{I_\mathrm{r} K N^2}{N^2 I_\mathrm{r} I_\mathrm{u} + I_\mathrm{u}^2}}\, p_\mathrm{ext} + \tau_\mathrm{u,op}. \end{aligned} \tag{13}$$

The low complexity of (13) allows to derive pocket-calculator-ready design equations as performed in the next Sec. II-D. However, the designer should monitor the deviation from (12). E.g. for $\Delta<\frac{\pi}{2\omega}$ (13) makes an error w.r.t. (12) of $\left(\hat{\tau}_\mathrm{u,peak,0}-\hat{\tau}_{\mathrm{u,peak},\Delta}\right)/\left(\hat{\tau}_{\mathrm{u,peak},\Delta}-\tau_\mathrm{u,op}\right)\in[0,0.06]$ and for $\Delta\to\frac{\pi}{\omega}$ the error approaches $\pi/4$.

To evaluate the validity of the undamped assumption, note that significant spring damping B_s induces an instantaneous torque response. E.g., $\tau_\mathrm{u,imp,0}(0^+)=(B_\mathrm{s}/I_\mathrm{u})p_\mathrm{ext}$. Furthermore, we have found the influence of motor damping B_r to negligibly increase $\tau_\mathrm{u,peak}$. However, link damping B_u reduces $\tau_\mathrm{u,peak}$. We have restricted our analysis to $a<1$ or $\Delta<\pi/\omega$, which states that the contact time is shorter than half of a free system oscillation. For this case the amplitude of the undamped system response is dominated by $G(t)$. In practice, the zero-damping approximation represents the worst-case for systems where damping is not deliberately introduced, and its accuracy can be verified using (6) or(7).

C. Sensitivity and Uncertainty

Sensitivity of $\hat{\tau}_{\mathrm{u,peak},\Delta}$ and $\hat{\tau}_\mathrm{u,peak,0}$ to its parameters z_i are shown in Tab. I. Uncertainty is evaluated via the Taylor expansion. Under the assumption of independently varied z_i

TABLE I
PARTIAL DERIVATIVES

z_i	$\frac{\partial\hat{\tau}_\mathrm{u,peak,0}}{\partial z_i}\frac{z_i}{\hat{\tau}_\mathrm{u,peak,0}}$	$\frac{\partial\hat{\tau}_{\mathrm{u,peak},\Delta}}{\partial z_i}\frac{z_i}{\hat{\tau}_{\mathrm{u,peak},\Delta}}$
I_r	$\frac{1}{2}$	$\frac{I_\mathrm{u}\omega^2-K}{4I_\mathrm{u}\omega^2}\left[\pi a\tan\left(\frac{\pi a}{2}\right)-\frac{6a^2-2}{1-a^2}\right]$
I_u	$\frac{-I_\mathrm{r}N^2-2I_\mathrm{u}}{2(I_\mathrm{r}N^2+I_\mathrm{u})}$	$\frac{K}{2\omega^2 I_\mathrm{u}}\left(\frac{\pi a}{2}\tan\left(\frac{\pi a}{2}\right)+\frac{a^2+1}{a^2-1}\right)-\frac{K}{\omega^2 N^2 I_\mathrm{r}}$
N	1	$\frac{I_\mathrm{u}\omega^2-K}{2I_\mathrm{u}\omega^2}\left[\pi a\tan\left(\frac{\pi a}{2}\right)-\frac{6a^2-2}{1-a^2}\right]$
K	$\frac{1}{2}$	$\frac{2(a^2+1)}{4(1-a^2)}-\frac{\pi a}{4}\tan\left(\frac{\pi a}{2}\right)$
p_ext	1	1
Δ	0	$\frac{2a^2}{1-a^2}-\frac{a\pi}{2}\tan\left(\frac{\pi a}{2}\right)$

with mean $\mu(z_i)$ and standard deviation $\sigma(z_i)$ the mean $\mu_{\mathrm{peak},j}$ and $\sigma_{\mathrm{peak},j}$ of $\hat{\tau}_{\mathrm{u,peak},j}$ with $j\in\{0,\Delta\}$ follow from [27] as

$$\mu_{\mathrm{peak},j} = \hat{\tau}_{\mathrm{u,peak},j}(\mu(z_i)) + \frac{1}{2}\sum_{i=1}^{5}\frac{\partial^2\hat{\tau}_{\mathrm{u,peak},j}(\mu(z_i))}{\partial z_i^2}\sigma(z_i)^2 \tag{14}$$

$$\sigma_{\mathrm{peak},j} = \sqrt{\sum_{i=1}^{5}\left(\frac{\partial\hat{\tau}_{\mathrm{u,peak},j}(\mu(z_i))}{\partial z_i}\right)^2\sigma(z_i)^2} \tag{15}$$

D. Robustness Against Specified Impacts

We demand that $\tau_\mathrm{u,peak}$ be less than the maximum allowable gearbox interface torque $\tau_\mathrm{u,max}$ when exposed to the maximum impulse $p_\mathrm{ext,max}$ while at maximum the maximum operational torque $\tau_\mathrm{u,op,max}$ is present as

$$\tau_\mathrm{u,peak}(p_\mathrm{ext,max},\tau_\mathrm{u,op,max}) \leq \tau_\mathrm{u,max}. \tag{16}$$

With (13), (16) is solved for K as

$$K \leq {I_\mathrm{u}}^2\left(\frac{1}{I_\mathrm{u}}+\frac{1}{N^2 I_\mathrm{r}}\right)\left(\frac{\tau_\mathrm{u,max}-\tau_\mathrm{u,op,max}}{p_\mathrm{ext,max}}\right)^2. \tag{17}$$

The required energy capacity of the spring for impact robustness $E=\frac{1}{2}Kq_\mathrm{s,imp}^2$ follows with the maximum additional deflection $q_\mathrm{s,imp}=(\tau_\mathrm{u,max}-\tau_\mathrm{u,op,max})/K$ as

$$E \geq \frac{1}{2{I_\mathrm{u}}^2}\left(\frac{1}{I_\mathrm{u}}+\frac{1}{N^2 I_\mathrm{r}}\right)^{-1} p_\mathrm{ext,max}^2. \tag{18}$$

E. Robustness Against Maximum Motor Speed

In case no data on the maximum expected impulse is available, an impact with the stationary environment that stops the link at maximum actuator velocity $\dot{q}_\mathrm{u,max}$ is a good engineering practice. This is equivalent to an inelastic impact and inequality (17) can be rewritten with $p_\mathrm{ext,max}=I_\mathrm{u}\dot{q}_\mathrm{u,max}$ as

$$K \leq \left(\frac{1}{I_\mathrm{u}}+\frac{1}{N^2 I_\mathrm{r}}\right)\left(\frac{\tau_\mathrm{u,max}-\tau_\mathrm{u,op,max}}{\dot{q}_\mathrm{u,max}}\right)^2. \tag{19}$$

Consequently, in this case, we require the following E:

$$E \geq \frac{1}{2}\left(\frac{1}{I_\mathrm{u}}+\frac{1}{N^2 I_\mathrm{r}}\right)^{-1}\dot{q}_\mathrm{u,max}^2. \tag{20}$$

For the case where additionally no estimate on I_u is available, we use the conservative limit case $I_\mathrm{u} \to \infty$ on (19) and (20) as

$$K \leq \frac{1}{N^2 I_\mathrm{r}} \left(\frac{\tau_\mathrm{u,max} - \tau_\mathrm{u,op,max}}{\dot{q}_\mathrm{u,max}} \right)^2, \tag{21}$$

$$E \geq \frac{1}{2} N^2 I_\mathrm{r} \dot{q}_\mathrm{u,max}^2. \tag{22}$$

F. Discussion and Comparison

While (17) and (18) describe a general case where p_ext is known, the inequalities (19)-(22) limit K and E for a perfectly inelastic collision of the link at maximum speed with a stationary object.

We make the assumption of $\tau_\mathrm{u,op} < \tau_\mathrm{u,op,max}$; when $\tau_\mathrm{u,op}$ is mainly influenced by the control action, this corresponds to an either bounded control response or no control response at all to the short-contact-time impact. A worst-case assumption for $\tau_\mathrm{u,op,max}$ can be the maximum torque capacity of the motor at the gearbox output.

Inequality (18) relates E to an increase in the kinetic energy of a resting system with inertia $(I_\mathrm{u}{}^2(1/I_\mathrm{u} + 1/N^2 I_\mathrm{r}))$ accelerated by $p_\mathrm{ext,max}$, inequalities (20) and (22) relate E to the kinetic energy of a system with inertia $(1/I_\mathrm{u} + 1/N^2 I_\mathrm{r})^{-1}$ at velocity $\dot{q}_\mathrm{u,max}$. Inequality (22) describes the case in which the kinetic energy of the reflected motor inertia $N^2 I_\mathrm{r}$ shall be fully stored in E after the link is completely stopped. While increasing I_u benefits (17) and (18) by minimizing spring energy absorption, it negatively affects (19) and (20) by hindering acceleration after the impact. Inequalities (21) and (22) are the limit case where this post impact acceleration is not possible.

The computation of E is a good way to understand the robustness requirement. In general, it is not sufficient for spring dimensioning but if $\tau_\mathrm{u,op,max} = 0$ and $\tau_\mathrm{u,max}$ was motivated only by the spring. Interestingly, for all (18),(20) and (22) E is independent of either K or $(\tau_\mathrm{u,max} - \tau_\mathrm{u,op,max})$.

In conclusion, our limit on K for specified impacts (17) can be used with more general collision dynamics with moving contact partners, while the inequality for an inelastic collision of the link at maximum speed (21) does not depend on I_u or prior knowledge of $p_\mathrm{ext,max}$.

III. Actuator Implementation with a Use Case

This section applies (17), (18), (21) and (22) to a proposed actuator for humanoid running. First, the requirements and structure of the actuator are introduced. Then the spring implementation and the torque-overload breakaway disk are described.

A. Use Case and Requirements

The actuator is designed for the hip of a running humanoid with a weight of $50\,\mathrm{kg}$ and a height of $1.5\,\mathrm{m}$. It is integrated into the joint to directly attach the robot links, eliminating additional bearings. Design requirements include 1) internal torque measurement; 2) gearbox protection against falls/mishandling; 3) structural capacity to withstand cross-axis moments; and 4) dissipation of generated heat. We want to achieve a performance similar to available off-the-shelf components and consider a maximum joint velocity of $10\,\mathrm{rad/s}$ and a maximum joint torque of $120\,\mathrm{Nm}$. Regarding the impulsive impact load on the actuator, we model the running motion as a succession of single-leg jumps and assume a rigid-link robot that impacts the ground with a vertical velocity of $2.5\,\mathrm{m/s}$. We model the initial impact transient as a fully elastic collision of the unsprung mass of $8\,\mathrm{kg}$ representing a single leg and an effective lever length of $0.3\,\mathrm{m}$ of the ground reaction force to the hip joint central axis. With these ground collision parameters we compute a maximum imparted impulse of $12\,\mathrm{Nm\,s}$. Additionally, we assume $\tau_\mathrm{u,op,max} = 30\,\mathrm{Nm}$ close to the end of the flight phase. In short, the performance requirements are the following:

- maximum joint velocity ($\dot{q}_\mathrm{u,max}$) = $10\mathrm{rad/s}$
- maximum joint torque ($\tau_\mathrm{u,max}$) = $120\ \mathrm{Nm}$
- maximum impact impulse ($p_\mathrm{ext,max}$) = $12\ \mathrm{Nm\,s}$

Calculation with $p_\mathrm{ext,max}$ from the requirement, actuator parameters in the following subsection, and assumed humanoid leg inertia $I_\mathrm{u,humanoid} = 1\,\mathrm{kgm}^2$ results in limit values of K and E of $6.4 \times 10^2\,\mathrm{Nm/rad}$ and $6.3\,\mathrm{J}$ from (17) and (18) or $8.4 \times 10^2\,\mathrm{Nm/rad}$ and $4.8\,\mathrm{J}$ from (21) and (22). We target $K = 6.2 \times 10^2\,\mathrm{Nm/rad}$ for our design to leave margin for manufacturing errors to the most restricting limit and verify (13) with (6) and assumed worst-case friction values of $B_\mathrm{r} = 0.001\,\mathrm{Nm/s}$, $B_\mathrm{s} = 0.01\,\mathrm{Nm/s}$ and $B_\mathrm{u} = 0\,\mathrm{Nm/s}$ and compute a maximum error of 1%. With the result from (17), our method is applicable for $\Delta < 36\,\mathrm{ms}$ which is in the range of biomechanically expected impact durations [2],[3].

B. General Assembly

From the requirements in Sec. III-A, we generate the detailed design implementation as shown in Fig. 3. The main elasticity is provided by the spring that connects the output flange to the gear output assembly, where an iC-Haus MU150 sensor is mounted to measure the spring deflection. Both spring and sensor are described in Sec. III-C. The gear output assembly is, in turn, connected to the gearbox via the torque-overload breakaway disk, described in Sec. III-D. We use a two-stage $N = 25$ Neugart PLE series planetary gearbox, with annular gears fixed to the stator housing, the gear carrier as output, and the sun gear as input, which is directly connected to the rotor. Two individual bearings decouple the stator housing from the rotor and the output flange. An iC-Haus MU200 sensor measures the absolute output position. The electromagnetic motor torque is provided by a TQ ILM85x23 in a star-parallel configuration. Total weight is $2.5\,\mathrm{kg}$ and rotor inertia $I_\mathrm{r} = 1.54 \times 10^{-4}\,\mathrm{kgm}^2$.

Both the high-diameter central bearing and the closely placed mounting and output flanges ensure high cross-axis torque and force stability. The directly measured spring deflection enables torque measurement. Heat transfer from the stator to the environment is facilitated through the stator housing, which is integral to the mounting flange and faces outward with a grooved surface.

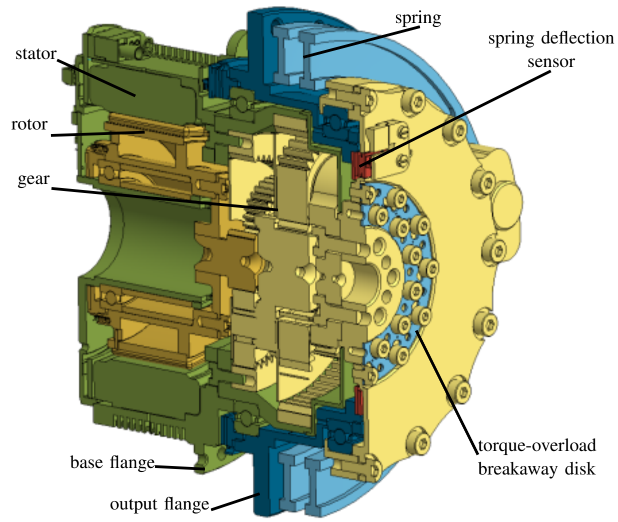

Fig. 3. Cross section of the presented actuator, where non-rotating parts are colored in green; the rotor in orange; the gearbox and the gear output assembly in light yellow; the output flange in dark blue; and the spring and the overload torque breakaway disk in light blue.

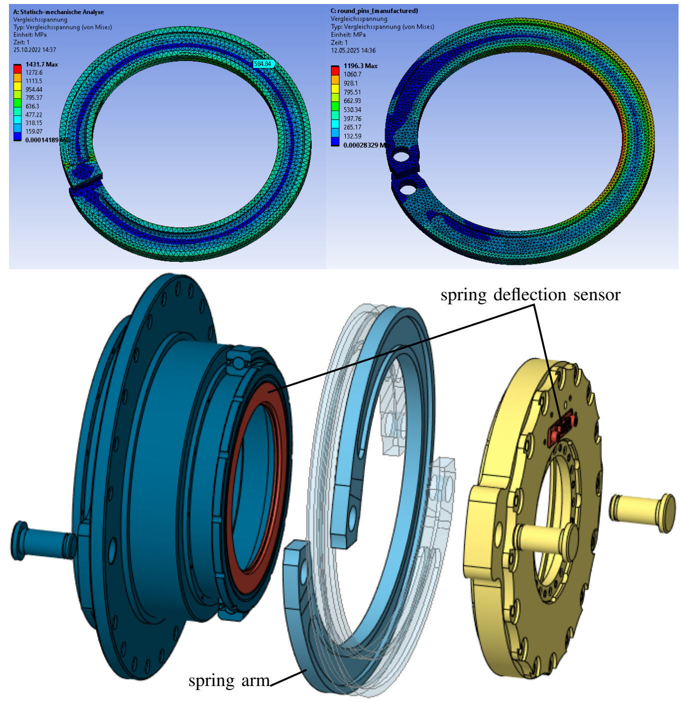

Fig. 4. **Top left**: FEM simulation of one arm of the helix spring with 6DoF fix constraint at the ends. **Top right**: FEM simulation of one arm of the helix spring with one free rotation constraint for the bolt interface. **Bottom**: Helical spring assembly. The two arms are fixed with bolts that allow torsional movement.

C. Custom-Designed Spring

We utilize the actuator housing's outer circumference for the spring, as typical axial springs, e.g., [18], would yield impractical dimensions and the planetary gearbox does not allow for a hollow-shaft spring [5]. The custom-designed spring in this letter consists of two helical spring arms with an I-beam cross-section that are mounted entwined with each other. When considering a perfectly stiff mounting of the ends of the spring arms, the constant diameter ensures an even loading of the spring arm. This even loading causes a constant stress distribution over the spring circumference, as seen on the top left of Fig. 4. The I-beam cross section further increases material utilization. In our implementation shown on the top right and bottom of Fig. 4, the ends of the springs are mounted on bolts. The additional rotational degree of freedom eliminates the otherwise infeasible interface torque in the connecting flanges. Since the spring arms are not in one plane, axial forces in the $100\,\mathrm{N}$ range are generated by the rotational deflection. These forces are absorbed by an additional bearing.

The deflection of the spring is sensed by an encoder iC-Haus MU150 with its passive part mounted on the base flange and its active part mounted on the gear output assembly. Each spring arm weighs $120\,\mathrm{g}$ and is manufactured from high-strength 1.7108 steel. In total, the spring stiffness is predicted to be $6.2 \times 10^2\,\mathrm{Nm/rad}$.

D. Torque-Overload Breakaway Disk

To enhance the robustness in practice, we reserve installation space for an additional physical impact protection with a low-cost and easy-to-exchange metal-sheet breakaway disk as shown in Fig. 5. This allows the gearbox, typically representing the most expensive and fragile component, to be protected with minimal increase in weight and volume. We accept that manual maintenance is needed after the rare event which triggers the coupling.

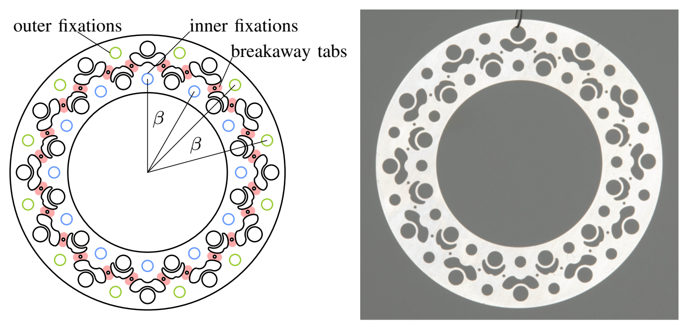

Fig. 5. Torque-overload breakaway disk. Left: schematic drawing highlighting the fixations and breakaway tabs. Right: Photograph of the fabricated disk with the thickness of $0.2\,\mathrm{mm}$.

The concept of the breakaway disk uses a single-part disk with tensile-stressed tabs that tear in the case of overload. Tearing ensures an instantaneous, easily detectable failure mode and it allows us to aim for a single dimensional stress loading. To ensure symmetric load-carrying capability, the disk is symmetric which implies only half of the tabs can experience tensile stress. Buckling shall ensure that the tabs under compression load do not significantly influence the tensile-stressed tabs.

In detail, the disk consists of both an inner and outer ring that connect to different shafts. Both rings are connected by convex tab-like regions that attach at neighboring fixation regions. There, dowel pins apply the load to the disk, while

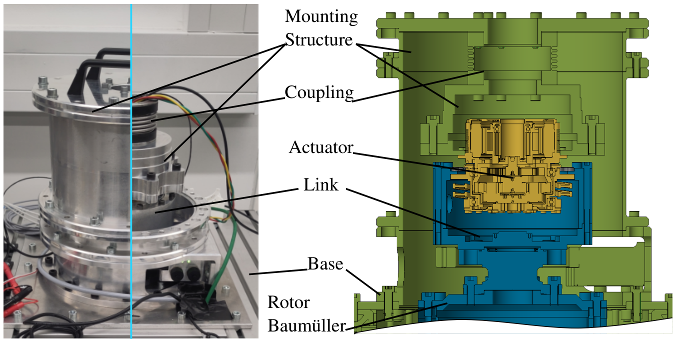

Fig. 6. Testbed configured for actuator impulse response tests. The mounting structure occludes both the tested actuator and the rotor of the Baumüller load motor.

additional screws prevent axial movement. Holes in the tabs deliberately concentrate the stress. Both thickness and the stress-concentration hole diameter are parameters that allow tuning the failure characteristics of the disk. For impulse experiments presented in Sec. IV-C, the desired breaking torque is between $100\,\mathrm{Nm}$ and $120\,\mathrm{Nm}$ which we have experimentally verified in five tests to be between $101\,\mathrm{Nm}$ and $111\,\mathrm{Nm}$. In this configuration with thickness $0.2\,\mathrm{mm}$ and 1.1274 steel the total weight amounts to $24\,\mathrm{g}$ including fixations.

In effect, our concept promises to protect the gearbox from torque overloading, while limited torque transfer capability remains after momentary overloading has occurred. If the mounting plane is accessible, the sheets can be easily exchanged. However, rigorous evaluation of our concept is still missing.

IV. Experimental Evaluation

A. General Testbed

All experiments use the same testbed in different configurations. A direct-drive load motor, Baumüller DST2-134MO45W-035, is mounted vertically within a table and connected to a contactless reference torque sensor, HBM K-T40B, at the output. Depending on the configuration, different connecting flanges connect the evaluated system to the torque sensor at one end and to a tolerance-compensating coupling, R+W BK1-200-53, at the other end. This coupling connects back to the table through a configurable tube-like assembly. Fig. 6 shows this assembly for the example of the actuator impulse response tests described in Sec. IV-C.

B. Spring Evaluation

The following experiments identify the spring stiffness: the load motor is commanded in position control, imposing a trajectory that alternates between increasing positive and negative deflection values, while each deflection is kept for $10\,\mathrm{s}$. We then decrease the maximum value in a symmetric fashion. Thus, every deflection level is reached twice, i.e., once before and once after reaching the maximum level. We log spring deflection measured via the integrated sensor and torque measured via the reference torque sensor.

Fig. 7 shows the result of a measurement and Tab. II provides details. Torque-deflection is smooth across the entire recorded deflection range and shows different stiffness for positive and negative deflections. At $100\,\mathrm{Nm}$ a slight change in stiffness is visible. For negative loads, the change in movement direction results in a loss of torque. This confirms the repeatability of the torque-deflection for the spring, which enables torque measurement via the spring despite non-linear effects. The lower-than-anticipated stiffness of the spring increases impact robustness above the limits of (17) and (21). We attribute the stiffness offset to inaccuracies in the manufacturing process as well as to play in the bolt interface. The latter might also cause the high hysteresis and sudden torque loss when unloading negative deflections. Overall, the spring has an energy capacity of $14\,\mathrm{J}$ or energy density of $58\,\mathrm{J/kg}$ and volumetric density of $0.14\,\mathrm{J/cm^3}$. While the former is comparable to the state of the art ranging between 60-80 $\mathrm{J/kg}$ the state of the art shows higher energy densities for axial mounting with 0.3-0.4 $\mathrm{J/cm^3}$ [18].

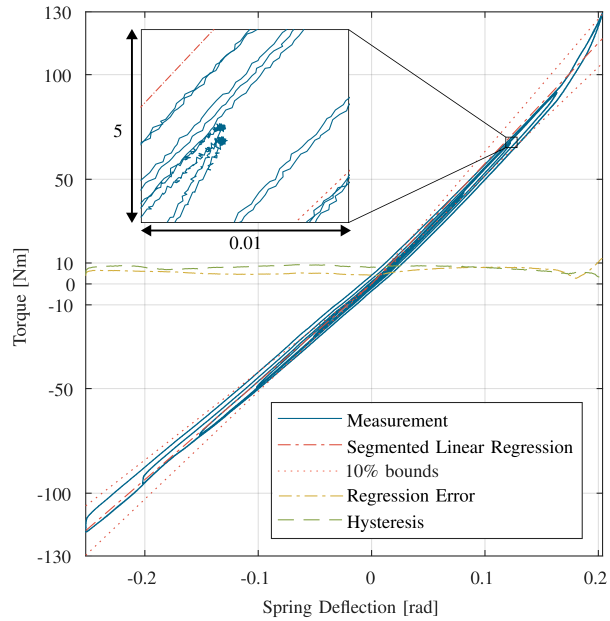

Fig. 7. Stiffness measurement of the spring. The position-controlled trajectory reaches separate holding positions, both before and after the maximum load of $130\,\mathrm{Nm}$. One extreme position that is reached twice is highlighted by example with a difference in torque smaller than $0.25\,\mathrm{Nm}$. Bold stiffness values from Tab. II are shown with 10% bounds.

TABLE II
Stiffness Measurement Results

Torque Range [Nm]	Stiffness [Nm/rad]	Hysteresis [Nm]
$[-60,\ 71]$	518	2.5
$[-118, 129]$	546	9
[0,129]	**575**	**9**
[-118, 0]	**467**	**9**

C. Actuator Impulse Response

This subsection experimentally validates that measured $\tau_{\mathrm{u,peak}}$ is proportional to p_{ext} when $\tau_{\mathrm{u,op}} = 0$ as stated (12) and (13) for the actuator presented at three

TABLE III
EXPERIMENT RESULTS

Exp.	#	$I_u[kgm^2]$	K[Nm/rad]	Δt[ms]	p_{ext}[Nms]	$\tau_{ext,peak}$[Nm]	$\tau_{u,peak}$[Nm]	$\mu(\eta_0)$	$\mu(\eta_\Delta)$	$\sigma(\eta_\Delta)$	χ^2_Δ
S1	81	0.14	575	[5, 20]	[0.18, 3.08]	[14.0, 243.4]	[4.9, 84.3]	0.16	0.11	0.03	1.50
S2	99	0.14	575	[25, 35]	[0.18, 3.07]	[8.1, 195.0]	[4.3, 82.7]	0.25	0.10	0.03	1.26
S3	81	0.21	575	[5, 20]	[0.18, 3.08]	[14.0, 243.4]	[3.8, 68.3]	0.11	0.07	0.03	0.59
S4	132	0.21	575	[25, 40]	[0.18, 3.07]	[7.0, 194.7]	[3.1, 66.5]	0.21	0.05	0.03	0.33
S5	89	0.29	575	[5, 20]	[0.18, 3.08]	[14.3, 243.4]	[2.9, 55.6]	0.06	0.02	0.04	0.15
S6	149	0.29	575	[25, 40]	[0.18, 3.08]	[7.0, 195.0]	[2.4, 54.4]	0.16	-0.00	0.04	0.13
S7	48	0.14	467	[5, 15]	[0.18, 2.21]	[18.7, 241.3]	[5.7, 70.2]	0.18	0.15	0.03	2.46
S8	99	0.14	467	[20, 30]	[0.17, 3.08]	[9.4, 243.6]	[5.2, 100.1]	0.24	0.11	0.02	1.60
S9	48	0.21	467	[5, 15]	[0.18, 2.21]	[19.2, 240.8]	[5.4, 55.2]	0.09	0.06	0.08	0.88
S10	132	0.21	467	[20, 35]	[0.18, 3.08]	[8.1, 243.4]	[4.8, 76.4]	0.19	0.04	0.07	0.70
S11	90	0.29	467	[5, 20]	[0.18, 3.08]	[14.3, 243.1]	[4.5, 59.9]	0.04	-0.01	0.11	1.09
S12	112	0.29	467	[25, 35]	[0.18, 3.07]	[8.1, 194.5]	[3.9, 58.6]	0.15	-0.03	0.09	0.88

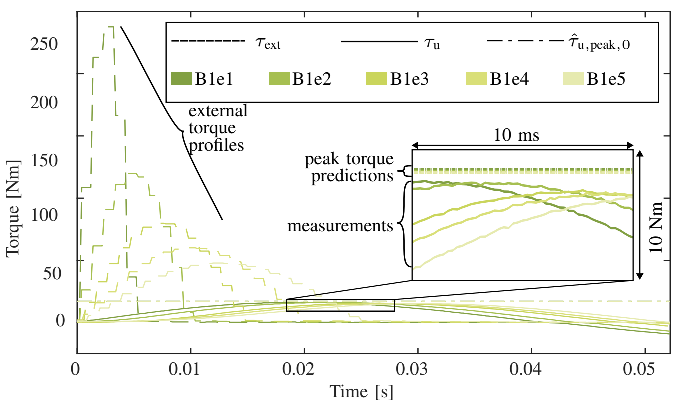

Fig. 8. Simulated impact experiment batch B1 with similar impulse for all experiments, $p_{ext} \approx 0.76\,\mathrm{Nms}$. External torque τ_{ext}, system torque response τ_u and the theoretical limit $\hat{\tau}_{u,peak,0}$ are shown for 5 different contact times Δ.

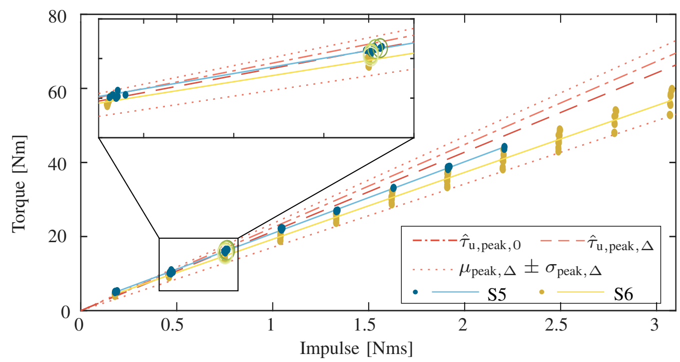

Fig. 9. Measured peak torque $\tau_{u,peak}$ over external Impulse p_{ext} for positive impulse with $K = 575\,\mathrm{Nm/rad}$ and $I_u = 0.29\,\mathrm{kgm}^2$. The model predictions $\hat{\tau}_{u,peak,0}$ and $\hat{\tau}_{u,peak,\Delta}$ and $\mu_{u,peak,0} \pm \sigma_{u,peak,0}$ are shown where $\Delta = \pi/(2\omega)$ and $\sigma(\Delta) = \pi/(2\omega)$. The two sets differ by Δ. Experiments B1 also shown in Fig. 8 are highlighted with green circles.

different settings of I_u. In the experiment setup, the complete actuator, including spring and torque-overload breakaway disk, is mounted. We measure τ_u via spring deflection by applying a fifth-order polynomial to the measurement data in Fig. 7 to account for the spring nonlinearities. The load motor is operated in feedforward torque control mode with a sample time of $1\,\mathrm{ms}$. Additional weights are used to vary I_u and mechanical parameters are taken from datasheets and CAD data, i.e., $I_{u,testbench} \in \{0.14\,, 0.21\,, 0.29\,\}\mathrm{kgm}^2$ and the values for I_r and N are given in Sec. III-B.

In several experimental batches B*, we apply sinusoidal torque pulses to a resting system with similar values of p_{ext}, but varying contact durations $\Delta \in [5\,\mathrm{ms}, \pi/\omega]$ and respective external peak torques $\tau_{ext,peak} < 250\,\mathrm{Nm}$. For our peak torque predictions, we use the boldly printed stiffnesses from Tab. II. Fig. 8 shows the exemplary time evolution within batch B1. Trapezoidal integration is used to calculate the transmitted momentum p_{ext}. In response to simulated impacts τ_u increases in a sinusoidal fashion to similar values $\tau_{u,peak}$ in all 5 experiments, despite the external peak torque being varied by a factor of five. The experiments differ slightly in the transferred impulse due to uncertainties in the feedforward torque command of the load motor.

In total, 1210 experiments are conducted. They are grouped into 12 sets S1-S12 depending on Δ, with threshold value of $\frac{\pi}{2\omega}$, deflection direction and respective stiffness and inertia setting. We evaluate the measurements via the relative errors η_j as $\eta_j = \frac{\tau_{u,peak,j} - \tau_{u,peak}}{\hat{\tau}_{u,peak,j}}, j \in \{0, \Delta\}$ and additionally use reduced $\chi^2_\Delta = \frac{1}{v}\sum\left(\frac{\tau_{u,peak,\Delta} - \tau_{u,peak}}{\sigma_{peak,\Delta}}\right)^2$ with v being the number of experiments and where regarding $\sigma(z_i)$ we use 10% for I_r, I_u and K, 1% for p_{ext} and $1\,\mathrm{ms}$ for Δ. Tab. III shows a summary of all sets with corresponding mean $\mu(\eta_j)$ and standard deviation $\sigma(\eta_\Delta)$.

Fig. 9 highlights sets S1-S2 and S5-S6 together with $\hat{\tau}_{u,peak,0}$ and $\hat{\tau}_{u,peak,\Delta}$ with added $\sigma_{peak,\Delta}$. For all sets, a linear relationship of $\tau_{u,peak}$ with p_{ext} is observed. The error η_0 increases on average with higher Δ while for η_Δ this relationship is not observed. Experiments in the negative direction and $K = 467\,\mathrm{Nm/rad}$ show less correlation with our model. We speculate, that the unsymmetrical hysteresis of our spring is a likely cause. Overall, we observe a general trend of decreasing η_Δ and χ^2_Δ with increasing I_u for both stiffness values. We speculate that this is due to link-side friction. From this, we deduce that extrapolation to $I_\text{u,humanoid}$ is possible.

In total, our observed data agree with the linear relationship of $\tau_\text{u,peak}$ and p_ext predicted by (12) for short-contact-time impacts with $\Delta < \frac{\pi}{\omega}$.

V. Conclusions

The maximum gearbox interface torque of short-contact-time impacts within an actuator with specified link and reflected rotor inertia follows from the transferred momentum and contact duration. We have analyzed this relation and provide a contact time limit and sensitivity to actuator parameters. Further we have derived worst-case closed-form design equations that are compatible with simple pocket-calculator use and provide explicit bounds on both actuator stiffness and spring energy capacity. These design equations have been used to guarantee that the target actuator cannot generate self-damaging impacts when interacting with a passive environment during the specified highly dynamic actuation task such as humanoid running. We fabricated the actuator prototype implementing the proposed design method, where a $14\,\text{J}$ spring protects against self-inflicted impacts and provides torque sensing. Furthermore, a torque-overload breakaway disk provides an additional safety layer against off-nominal impacts that could result from an active environment or failures in different subsystems of the robotic system. In experiments with simulated impacts on our actuator, the interface torque prediction correlates with the measurement result.

In future work, we will increase the manufacturing accuracy of the spring, reduce the play in the spring mounting, study the fatigue behavior of the torque-overload breakaway disk, and integrate the actuator into an actual robot. Further, we will investigate how well the proposed SEA model represents short-contact-time impact response of QDDs with their physical gearbox elasticity as stiffness.

References

[1] K. Fründ, F. Beck, A. Shu, F. Loeffl, and J. Lee, "Bipedal running: Bioinspired fundamentals for versatile humanoid robot locomotion," in *IEEE/RAS International Conference on Humanoid Robots*, 2023, pp. 1–8.

[2] J. A. Dickinson, S. D. Cook, and T. M. Leinhardt, "The measurement of shock waves following heel strike while running," *Journal of Biomechanics*, vol. 18, no. 6, pp. 415–422, 1985.

[3] D. E. Lieberman, M. Venkadesan, W. A. Werbel, A. I. Daoud, S. D'Andrea, I. S. Davis, R. O. Mang'Eni, and Y. Pitsiladis, "Foot strike patterns and collision forces in habitually barefoot versus shod runners," *Nature*, vol. 463, no. 7280, pp. 531–535, 2010.

[4] S. Haddadin, T. Laue, U. Frese, S. Wolf, A. Albu-Schäffer, and G. Hirzinger, "Kick it with elasticity: Safety and performance in human–robot soccer," *Robotics and Autonomous Systems*, vol. 57, no. 8, pp. 761–775, 2009.

[5] F. Negrello, M. Garabini, M. G. Catalano, J. Malzahn, D. G. Caldwell, A. Bicchi, and N. G. Tsagarakis, "A modular compliant actuator for emerging high performance and fall-resilient humanoids," in *IEEE/RAS International Conference on Humanoid Robots*, 2015, pp. 414–420.

[6] P. M. Wensing, A. Wang, S. Seok, D. Otten, J. Lang, and S. Kim, "Proprioceptive Actuator Design in the MIT Cheetah: Impact Mitigation and High-Bandwidth Physical Interaction for Dynamic Legged Robots," *IEEE Transactions on Robotics*, vol. 33, no. 3, pp. 509–522, 2017.

[7] J. Yamaguchi, A. Takanishi, and I. Kato, "Experimental development of a foot mechanism with shock absorbing material for acquisition of landing surface position information and stabilization of dynamic biped walking," in *IEEE International Conference on Robotics and Automation*, vol. 3, 1995, pp. 2892–2899.

[8] S. Wolf and A. Albu-Schaffer, "Towards a robust variable stiffness actuator," in *IEEE/RSJ International Conference on Intelligent Robots and Systems*, 2013, pp. 5410–5417.

[9] G. Pratt and M. Williamson, "Series elastic actuators," in *IEEE/RSJ International Conference on Intelligent Robots and Systems.*, vol. 1, 1995, pp. 399–406.

[10] D. Calzolari, C. Della Santina, and A. Albu-Schäffer, "Exciting families of passive gaits in an elastic quadruped via natural motion manifold control," *International Journal of Robotics Research*, 2025.

[11] D. Robinson, J. Pratt, D. Paluska, and G. Pratt, "Series elastic actuator development for a biomimetic walking robot," in *IEEE/ASME International Conference on Advanced Intelligent Mechatronics*, 1999, pp. 561–568.

[12] W. Townsend and J. Salisbury, "Mechanical bandwidth as a guideline to high-performance manipulator design," in *IEEE International Conference on Robotics and Automation*, vol. 3, 1989, pp. 1390–1395.

[13] S. Seok, A. Wang, M. Y. Chuah, D. J. Hyun, J. Lee, D. M. Otten, J. H. Lang, and S. Kim, "Design Principles for Energy-Efficient Legged Locomotion and Implementation on the MIT Cheetah Robot," *IEEE/ASME Transactions on Mechatronics*, vol. 20, no. 3, pp. 1117–1129, 2015.

[14] Maxon International ltd., "Datasheet HEJ 90-48-90," 2025. [Online]. Available: https://global.maxongroup.com/hubfs/Team_HQ_Global/10_Robotics/Datasheet_HEJ_90_48_140_rev2.0.pdf

[15] K. Kojima, Y. Kojio, T. Ishikawa, F. Sugai, Y. Kakiuchi, K. Okada, and M. Inaba, "Drive-Train Design in JAXON3-P and Realization of Jump Motions: Impact Mitigation and Force Control Performance for Dynamic Motions," in *IEEE/RSJ International Conference on Intelligent Robots and Systems*, 2020, pp. 3747–3753.

[16] A. Shu, C. Raschel, M. Keppler, A. Wedler, and M. Görner, "Impact Robustness Versus Torque Bandwidth: A Design Guide for Differential Elastic Actuators," *IEEE Transactions on Robotics*, vol. 40, pp. 3657–3675, 2024.

[17] G. Carpino, D. Accoto, F. Sergi, N. Luigi Tagliamonte, and E. Guglielmelli, "A novel compact torsional spring for series elastic actuators for assistive wearable robots," *Journal of Mechanical Design*, vol. 134, no. 12, p. 121002, 2012.

[18] Z. Bons, G. C. Thomas, L. Mooney, and E. J. Rouse, "An Energy-Dense Two-Part Torsion Spring Architecture and Design Tool," *IEEE/ASME Transactions on Mechatronics*, pp. 1–12, 2023.

[19] A. Edsinger-Gonzales, "Design of a Compliant and Force Sensing Hand for a Humanoid Robot:," in *International Conference on Intelligent Manipulation and Grasping*, 2004.

[20] M. Lauria, M. Legault, M. Lavoie, and F. Michaud, "Differential elastic actuator for robotic interaction tasks," in *IEEE International Conference on Robotics and Automation*, 2008, pp. 3606–3611.

[21] C. Lee and S. Oh, "Configuration and performance analysis of a compact planetary geared Elastic Actuator," in *Annual Conference of the IEEE Industrial Electronics Society*, 2016, pp. 6391–6396.

[22] Z. J. Jackowski and A. Young, "Transmission with Integrated Overload Protection for a Legged Robot," US Patent 20 200 256 399A1, 2020.

[23] J. Reinecke, A. Dietrich, A. Shu, B. Deutschmann, and M. Hutter, "A Robotic Torso Joint With Adjustable Linear Spring Mechanism for Natural Dynamic Motions in a Differential-Elastic Arrangement," *IEEE Robotics and Automation Letters*, vol. 7, no. 1, pp. 9–16, 2022.

[24] F. Ostyn, "Impact-resilient high performance robot actuators via lightweight overload clutch design with wedged rollers," in *IEEE/RAS International Conference on Humanoid Robots*, 2024, pp. 32–36.

[25] C. Lee, S. Kwak, J. Kwak, and S. Oh, "Generalization of Series Elastic Actuator Configurations and Dynamic Behavior Comparison," *Actuators*, vol. 6, no. 3, p. 26, 2017.

[26] I. Walker, "Impact configurations and measures for kinematically redundant and multiple armed robot systems," *IEEE Transactions on Robotics and Automation*, vol. 10, no. 5, pp. 670–683, 1994.

[27] H. H. Ku, "Notes on the use of propagation of error formulas," *Journal of Research of the National Bureau of Standards*, vol. 70C, Oct. 1966.